An experimental and numerical investigation of frictional losses and film thickness for four cylinder liner variants for a heavy duty diesel engine

Andrew Spencer[1*], Emin Yusuf Avan[2], Andreas Almqvist[1], Rob S Dwyer-Joyce[2], and Roland Larsson[1]

[1]Division of Machine Elements, Luleå University of Technology, Luleå, Sweden
[2]The Leonardo Centre for Tribology, Department of Mechanical Engineering, University of Sheffield, Sheffield, UK
[*]Corresponding author, email: andrew.spencer@ltu.se

Abstract

The piston ring pack is the single greatest contributor to mechanical losses in a Heavy Duty Diesel Engine (HDDE), accounting for 1.1-6.8% of the total losses. Therefore, the piston ring-cylinder liner contact is potentially the most rewarding area to study when attempting to reduce mechanical losses in a HDDE. In this work, four different HDDE cylinder liner variants have been tested to evaluate the lubricating conditions that occur when a section of top compression ring is reciprocated against them in a lubricated environment. Two of the cylinder liners were traditional grey cast iron and plateau honed with different honing angles, one had ANS Triboconditioning® applied and the last was plasma sprayed with a stainless steel and ceramic coating, then honed. An experimental test rig was used where friction and film thickness was recorded, by means of an ultrasonic technique. A numerical model was also developed to calculate the friction and film thickness. Comparisons are made between the simulation and experiment, and the four cylinder liner variants are also evaluated. It was found that both simulation and experiment could differentiate between all surfaces and the results from the model and experiment also correlated well with each other. A lower plateau average surface roughness, as exhibited by the ANS Triboconditioning® and plasma liners, led to a significant reduction in friction.
Keywords: cylinder liner , ultrasound , tungsten disulphide , piston ring , honing

1 Introduction

Fuel efficiency is one of the most important areas of automotive vehicle research and development today, with rising fuel costs, energy security and environmental concerns being at the forefront of customers and legislators minds. Heavy Duty Diesel Engines (HDDE) are the primary source of mechanical power generation in today's trucks and buses and this is likely to continue for the foreseeable future. In 2010 the global demand for diesel fuel was 16 million barrels of oil per day, in 2040 this is predicted to be 26 million barrels per day, an increase of 60% [1]. EU transport still depends on oil and oil products for 96% of its energy needs [2]. Although larger trucks and truck efficiency will increase, growing worldwide GDP will increase the need for road transportation and road congestion will increase fuel use further. In the 2011 European Commission White Paper on transport [2], a reduction of at least 60% of greenhouse gas emissions from transport by 2050, with respect to 1990 levels, was called for. The report concludes that acting on vehicles' efficiency through new engines,

materials and design will help in the reduction of oil dependence, the competitiveness of Europe's automotive industry as well as health benefits, especially improved air quality in cities. However, it is predicted that a considerable extent of the shipments over short and medium distances, i.e. below 300 km, and that 50% of shipments over 300 km will remain on trucks even in 2050. Also, there will be a greater push in cities to encourage the use of public transport with large fleets of urban buses. Therefore, the efficiency and frictional losses in a vehicles powertrain, particularly those in trucks and buses powered by a HDDE, are areas of great interest.

Only about 40% of the fuel energy consumed in a HDDE is converted to mechanical power [3]. The rest is lost to a combination of thermal and mechanical losses. Although the thermal losses are the greatest component, the mechanical friction losses are significant at between 4-15% of the total fuel energy [3]. Of these mechanical losses, the piston ring pack is the greatest single contributor, amounting to 1.1-6.8% of the total losses in a HDDE [3]. Hence the ring pack is possibly the most interesting area for consideration when trying to reduce mechanical friction in an engine.

Cylinder liner surface topography can be an important factor in the amount of piston ring-cylinder liner (PRCL) friction generated. Various authors have investigated the effect of surface roughness and topography on PRCL lubrication [4, 5]. Johansson et al. [6] showed through simulation that cylinder liner surfaces with a lower core roughness parameter, R_k, exhibit both lower film thickness and friction. In fired engine tests with a floating liner, Sato et al. [7] showed that a smoother surface reduced PRCL friction. However, with smoother surfaces more 'vertical flaws', or scuffing, became apparent on the liner and this led to increased oil consumption.

In this work, four distinct cylinder liners are investigated, each with different surface roughness and one with a low friction surface coating. The samples are investigated with both numerical simulations and in an experimental test rig, to aid in validating the numerical solution. Both friction and film thickness are simulated and measured. The friction is the primary parameter of interest, however the film thickness aids in understanding the friction results and allows a more in-depth comparison of the numerical and experimental solutions.

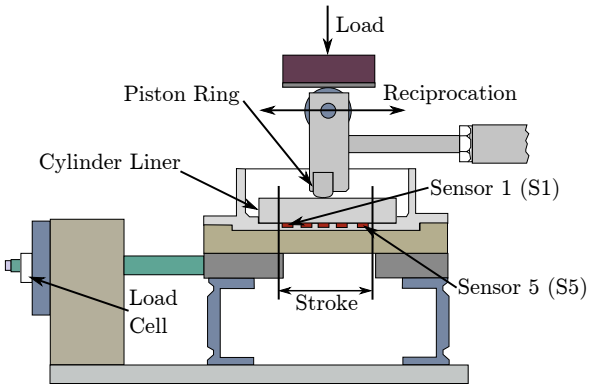

Figure 1: Plint TE-77 simulated piston ring-liner contact schematic.

This work has two objectives: firstly to see whether advanced surface topographies, with lower roughness and surface coatings, can reduce friction over more traditional topographies, and secondly to see whether numerical simulations can accurately predict the friction between the different surfaces. If possible, the numerical model could then be used to 'optimise' the surface roughness and investigate possibilities of even lower friction. It is the authors belief that this is the first time that both experimentally and numerically obtained film thickness has been used to evaluate different cylinder liner surface topography.

2 Experimental setup

The experimental setup and ultrasound measurement technique is the same as that used previously by the authors [8]. This work is referenced for a detailed description of the setup of the test rig and processing of the ultrasound data, however a more brief description of the setup will also be given here.

2.1 Test setup, specimens and lubricant

A Plint TE-77 high frequency reciprocating tribometer, schematically shown in Figure 1, was used in this work. The machine configuration consists of sections of piston ring and liner where the ring specimen reciprocates over the stationary liner sample. The normal load is applied via a spring-balance

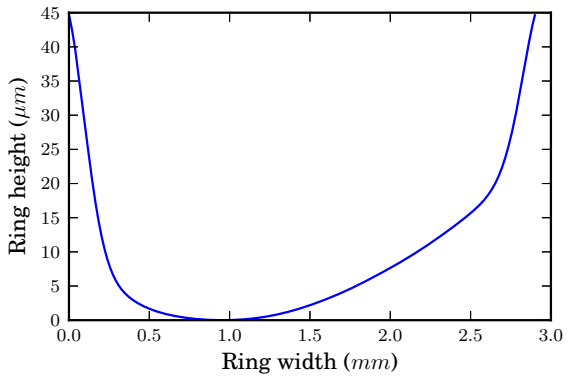

Figure 2: Top Compression Ring Profile. When fitted in an engine the right hand side faces towards the combustion chamber. In these tests, the right hand side faces towards the reciprocating arm.

through a lever and stirrup mechanism. The normal force is transmitted directly onto the ring section by means of a needle roller cam follower on a carrier head and a running plate on the loading stirrup. The whole assembly is mounted on flexible supports providing for free movement in horizontal directions, and connected to a stiff force transducer (Kistler type 9203) that measures tangential force in both directions.

A section of run-in cylinder liner and top compression ring from the same heavy duty diesel engine were used to create the contact. Four different cylinder liner samples were used with different surface topographies and material properties, these are discussed later in Section §4. Each cylinder liner sample measured 50 mm in length and 20 mm in width and was cut from a complete cylinder liner with a bore diameter of 130 mm. The piston ring was sectioned into a length of 45 mm. The width of the piston ring is 3 mm and it has an asymmetric barrel shaped face, as illustrated in Figure 2, with a chrome surface coating.

A lubricant bath was modified to hold the liner specimen. Six grub screws were used to secure the liner specimen in place; this allows for alignment of the liner in both the axial and lateral directions. To retain the ring section, a special ring holder attached to the carried head was manufactured from an original production piston. A ring section was clamped to the ring holder using two slotted plates either side of the ring holder and a grub screw in the centre. This clamping system bent the ring section and allowed it to conform over the liner section. The conformability between the ring and liner was checked using pressure paper and a good conformal contact was obtained [8].

2.2 Test conditions

For each of the four liner surfaces, tests were run for a range of speeds and loads. The load was varied from 40 N to 200 N in steps of 20 N and the speed was varied from 2.5 Hz to 17.5 Hz in steps of 2.5 Hz, giving 63 test points in total (7 speeds and 9 loads).

At this point it is of interest to make a comparison with the real engine operating conditions. The maximum piston speed at 1200 RPM is 10.5 m/s. At a peak combustion pressure of 200 bar, if this pressure is assumed to act entirely on the back of the top compression ring, the load on a section of ring of the size used in these tests (20 mm x 3mm) would be 1200N. This is the maximum speed and load that the top compression ring is subjected to in the engine. Therefore, the speed in these tests is representative of the reversal points, but not mid-stroke. Also, the load is representative of most of the engine cycle, but not around the region of peak combustion pressure. It would of course be of interest to run at higher speeds and loads, but the conditions used here were the upper limits of the capabilities of the test rig used in this study.

The stroke of the machine was set to 15 mm (the maximum value). The liner specimen was fully immersed in pure base oil without an additive package. The oil bath temperature was logged at a stable 22^{o}C throughout the tests. It is acknowledged that the lubricant temperature is unrepresentative of real engine running conditions. However, the primary goal of this work is to accurately and repeatably investigate different liner surface topographies rather than recreate engine running conditions. It was decided that running at a lower temperature, giving a higher viscosity and therefore higher film thickness would go some way towards compensating for the lower entraining speeds in the test rig compared to the real engine operating conditions. In addition, the large quantity of lubricant in the oil bath ensures that the inlet is always fully flooded allowing for good, accurate comparisons with the

Table 1: Sensor's location over the stroke for the liner samples.

		Distance from TDC (mm)			
Liner Sample		STD55	STD35	ANS	PL
TDC		0.00	0	0	0
Sensor Number	1	1.4	1.4	1.4	1.6
	2	4.1	4.3	4.2	4.7
	3	7.3	7.4	7.1	7.4
	4	10.4	10.2	9.7	10.0
	5	13.3	13.2	13.2	13.0
BDC		15.0	15.0	15.0	15.0

numerical model. It also serves in maintaining a stable temperature of the liner surface during the short tests.

2.3 Ultrasonic film thickness measurement

For over a decade, several methods have been developed and used to measure the thin oil film that forms under piston rings such as capacitance [9, 10, 11], resistance [12] and the laser induced fluorescence method [13, 14, 15]. However, these are all invasive methods meaning that they require penetration of the cylinder liner in order to measure the piston ring to cylinder liner film thickness. In this study, a non-invasive ultrasound technique based on sensing the reflections from the piston ring-liner contact was used. This technique has been recently applied to a hydraulic motor piston ring-liner [16], a motored engine [17] and a fired engine [18] to quantify the oil film thickness between piston ring and cylinder liner.

To generate ultrasonic waves, 10 MHz piezoelectric crystals with a width of 1.3 mm and a length of 2.5 mm were placed on the back side of each liner segment. Five such ultrasonic sensors were equally distributed along the axial length of the stroke, within millimetre precision. The positions of the sensors on the each liner sample are given in Table 1.

When these piezo elements are pulsed at high frequencies they generate and send ultrasonic waves through the inner liner surface. When the piston ring is within the sensing area, some of the incident wave is transmitted forward to the ring and the remainder is reflected back. The proportion that is reflected is known as the reflection coefficient, R, and varies with the acoustic properties of the materials and the stiffness of the layer, K. The response of a thin layer embedded between two materials is governed by a quasi-static spring model [19],

$$R = \frac{1}{\sqrt{1 + (2K/\omega z)^{\mathbf{2}}}} \tag{1}$$

where ω is the angular frequency of the ultrasound and z the acoustic impedance of the materials. For the case of liquid layer trapped between two flat surfaces, the stiffness of the layer can be related to its bulk modulus, B, and thickness, h, by $K = B/h$. Furthermore, the bulk modulus can be replaced using the relation, $B = \rho c^2$, where ρ and c are the speed of sound and density of the liquid layer (i.e. lubricant) respectively. This gives,

$$K = \frac{\rho c^2}{h} \tag{2}$$

If equation (2) is substituted into equation (1) and rearranged, this gives equation (3) where the layer thickness can be described in terms of reflection coefficient and acoustic properties of the oil and materials either side of the interface;

$$h = \frac{\rho c^2}{\pi f z}\sqrt{\frac{|R|^2}{1-|R|^2}}, \tag{3}$$

where f is the frequency of the ultrasonic pulse. In this work the acoustic impedance of the cast iron piston ring and liners, z, is 34.9 MRayl and speed of sound in base oil can be found in Table 2.

During the tests, the ultrasonic reflections were recorded as the piston ring passed over the sensing area. The reflection coefficients were created by normalizing measured reflections with a 'reference' reflection and then the spring model equation (3) was employed for each reflection coefficient to determine the oil film thickness. Practically, the air-liner interface was used as a reference interface because an almost complete reflection of incident wave occurs for this interface due to a high acoustic mismatch. Before testing, the inner liner surface was therefore cleaned (no oil present on the surface) and the reference signal for each individual sensor was recorded. More detail about ultrasound film thickness measurement and signal processing can be found in [20] and [8].

In the experiments, ultrasonic data from the sensors was simultaneously streamed into an ultrasonic pulsing unit via 5 channels. The unit consists of an ultrasonic pulsing and receiving card, a data acquisition card and digitising card. Each channel was pulsed at a repetition rate of 15k pulses/second. The data was digitised at 100 MHz with a 12 bit resolution.

3 Numerical model

A numerical model of the experiment has been developed in order to predict both the film thickness and friction that also are measured in the previously described experimental setup. As it is assumed that the piston ring-cylinder liner contact runs in the mixed lubrication regime for at least some of the stroke, a model must be developed that calculates both the hydrodynamic film pressure and asperity contact pressure.

The contact profile is first converging then diverging. This leads to that cavitation will occur along the trailing edge of the ring. In order to solve the Reynolds equation incorporating cavitation, a modified version of the Giacopini et al. [21] mass-conserving cavitation algorithm was used. More precisely, a two dimensional time dependent solution of an averaged form of the Reynolds equation was restated as a Linear Complimentary Problem (LCP).

$$\begin{aligned} \nabla \cdot (A_0 \nabla p_0) - \lambda \nabla \cdot (B_0) - \gamma \frac{\partial}{\partial t} \left(\bar{h}\right) \\ + \lambda \nabla \cdot (r B_0) + \gamma \frac{\partial}{\partial t} \left(r \bar{h}\right) = 0, \\ p_0 > 0, \\ r > 0, \\ p_0 r = 0. \end{aligned} \tag{4}$$

where p_0 is the averaged film pressure, r is the complementary variable and λ and γ are constants defined in the nomenclature. The advantage with the approach proposed by Giacopini et al. [21] is that the two unknowns become complementary throughout the whole domain. Existence and uniqueness of the solution follows by the rigorous mathematical analysis in Bayada et al. [22]. The advantage with the LCP formulation is that standard techniques can be used to solve the problem numerically, e.g. Lemke's pivoting algorithm. See e.g. the book by Cottle et al. [23]. This alleviates the problematics associated with discrete formulations that changes at the boundaries between the cavitated and the full film zones. Moreover, this solution technique finds the solution in a finite number of steps, hence issues related to iterative processes are avoided.

If $r = 0$ then the contact is fully flooded and a positive hydrodynamic pressure exists in the lubricant. If $r > 0$, there is no hydrodynamic pressure in the lubricant, physically the lubricant is cavitating here. r can be defined as follows;

$$r = 1 - \frac{\rho}{\rho_c} \tag{5}$$

where ρ is the density of the lubricant and ρ_c is the density of the lubricant at the cavitation pressure, which in this work is assumed to be atmospheric pressure. With equation (4) in this form, the film thickness is replaced with coefficients, A_0 and B_0 where,

$$A_0 = \begin{pmatrix} a_{11} & a_{12} \\ a_{21} & a_{22} \end{pmatrix} \text{ and } B_0 = \begin{pmatrix} b_1 \\ b_2 \end{pmatrix} \tag{6}$$

A_0 and B_0 are calculated for each of the surfaces under investigation. An explanation of the method to calculate these coefficients is given later in Section 4.1. The average film thickness parameter, $\bar{h}$, is defined as;

$$\bar{h} = h_0(x, \int_Y, t) + \frac{1}{l_1 l_2} \int h_r(x, y) dy, \tag{7}$$

where h_0 is the global separation between the piston ring and cylinder liner, h_r is the liner roughness, l_1 and l_2 are the length and width of the roughness measurement and Y is the domain of the local scale, which is further discussed in Section §4. The boundary conditions were defined as $p_0 = 0$ and $r = 1$ at the leading edge, trailing edge and sides of the contact which corresponds to fully flooded and zero pressure. Zero pressure boundary conditions were implemented as the ring is not subjected to gas pressures at either edge of the ring, as would be the case in a real engine. These boundary conditions are not representative of real engine operating conditions, but are used in these tests as they are

repeatable and known, as opposed to a starved inlet where the degree of starvation would be hard to measure experimentally.

The LCP problem, i.e. equation (4), was discretised using the finite difference method, with central differences in space for all terms except for $\nabla \cdot (rB_0)$ which was upwind differenced, to properly consider the hyperbolic nature of the problem inside cavitation zones. An explicit method built on the forward Euler method was used to discretise the problem in time. The solution domain, equation (4), was divided into 50 by 10 nodes (50 in the entraining direction, 10 across the width), which was found to make the film thickness and friction virtually independent of grid size. Such a coarse grid representation is made possible by incorporating the effect of surface roughness in the coefficients A_0, B_0 and $\bar{h}$. The problem was divided into 100 time steps. Increasing the number of time steps was found to only marginally affect the solution.

At the reversal point the value of r at all grid points was set to 1. The reason for this is as follows. As the ring slides a cavitated region is formed in the diverging outlet section of the ring. As the ring changes sliding direction at the reversal point, this cavitated region is now found in the inlet region. The ring must then slide far enough for new oil to enter the contact before a wedge of oil can be formed and hydrodynamic lift generated. This is a real physical phenomenon, however in the Plint test rig there is a large quantity of oil in the oil bath, unlike on the cylinder liner surface in a real engine. It is in these authors opinion that at the reversal point, in this lubrication situation, this oil rapidly replenishes into the diverging portion of the ring and fills what becomes the inlet region of the ring at reversal. There is no direct experimental evidence for this, however the rapid increase in ultrasonically measured film thickness as the ring moves away from the reversal point indicates that the inlet must be fully flooded with lubricant immediately after reversal. The physics of this oil flow is not modelled by the Reynolds equation. By setting r to 1 at the reversal points, the contact is artificially fully replenished with oil immediately. This is thought to properly simulate the mechanism described above.

Each time step is associated to a specific Plint spindle angle (θ) and the velocity of the piston ring was calculated from equation (8):

$$U = \pi N s \cdot \cos(\theta), \tag{8}$$

where N is the rotational speed of the Plint machine in Hz and s is the stroke length, which in these tests was 15 mm. Once the velocity is known a force balance equation is solved for the film thickness;

$$F_{HYD}(h) + F_{CP}(h) = F_{LOAD} \tag{9}$$

The hydrodynamically supported load, F_{HYD}, comes from integrating the hydrodynamic pressure found from equation (4). The asperity contact load, F_{CP}, is found from integrating the asperity contact pressure, P_{CP}, from the contact mechanics simulation result, presented in Figure 4, and F_{LOAD} is the applied load in the test.

The LCP problem (equation (4)) is solved using Lemke's Complementary Pivot algorithm with the LCP solver included in OpenOpt [24]. Once the force balance is solved the problem can be incremented one time step and the process repeated. The solution at the current time step depends on the previous one and the solver must be run through approximately 1.1 full cycles for the transients to fade out and to reach convergence with the previous cycle. Convergence is assumed to be reached when the film thickness and the derivative of the film thickness are within 1% of the previous cycle.

The friction force (f_{tot}) is calculated as the sum of viscous friction force f_{hyd} and boundary friction force f_{bd}. Boundary friction is calculated as;

$$f_{bd} = \mu \int_{\Omega} P_{CP} dA, \tag{10}$$

where μ is the dry friction coefficient and P_{CP} is the average asperity contact pressure, found from the contact mechanics model, see Figure 4. The boundary friction coefficient, taken from Table 3, was found by running a reciprocating test in the test apparatus described in Section 2.1, with a small quantity of lubricant present and at a very low speed to ensure that no hydrodynamic lubrication effect occurred. The values 30° each side of the reversal points (0° and 180°) are not included in the average, which translates to the first (and last) 3.75 mm of the stroke. The justification for this is that, in these friction tests, at the reversal points the stick-slip phenomenon occurs between the ring and liner

as the ring starts moving from stationary. This leads to a 'noisy' friction value before the measurement settles to a constant value. Of course, these reversals also occur in the actual tests, however due to the much higher speeds involved and some flex in the text rig, the ring breaks cleanly away from stationary along the liner surface and stick-slip does not occur, or at least to a much smaller degree. For these simulations we require the friction coefficient of boundary lubricated sliding, not of the stick-slip phenomenon. The values are presented in Table 3. Hydrodynamic friction is calculated as;

$$f_{hyd} = \int_{\Omega} \left(\eta \frac{U}{h} + \frac{h}{2} \frac{\partial p_0}{\partial x} \right) dA, \qquad (11)$$

where A is the area of the contact.

3.1 Lubricant properties

The ASTM D341 equation was used to calculate the lubricant viscosity at 22 °C;

$$log(log(\eta + 0.7)) = A - B \cdot log(T + 273.15), \quad (12)$$

where η is viscosity, A and B are constants and T is temperature. Using the values in Table 2, $A = 8.8686$ and $B = 3.4743$, giving a viscosity of 85.66 cSt or 0.072 $Pa \cdot s$, at 22°C. In the contact it is predicted that the temperature of the lubricant will be higher than that of the bulk lubricant due to shear heating. Therefore, the viscosity will be less in the contact than the value that has been calculated here. However, in the absence of a measured contact temperature or thermal model, such as in the one by Morris et al. [25], the bulk lubricant temperature and hence viscosity will be used in the numerical model.

Table 2: Properties of the lubricant used in the tests.

Density, ρ	843.4 kg/m^3
Kinematic Viscosity at 40°C, η	37 cSt
Kinematic Viscosity at 100°C, η	6.5 cSt
Longitudinal wave velocity, c	1440 m/s

4 Surfaces under investigation

Four different cylinder liner variants are investigated and compared in this work. 3D surface measurements of the four cylinder liners are shown in Figure 3. The surface measurements, taken with a Talysurf CLI 2000, were taken just of an area of plateau on the cylinder liner surface - any large honing grooves were avoided. These surfaces will be used to calculate homogenized coefficients A_0, B_0 and $\bar{h}$. As investigated previously by Spencer et al. [26], due to the large wavelength of the honing grooves in relation to the measurement and contact size, they should not be considered on the local scale and homogenized together with the surface roughness. However, this is somewhat of a limitation of this model, as any effect that the honing grooves have on the lubrication will not be simulated. Each of the measurements is 150x150 μm and 139x139 data points, with the exception of the ANS liner which measured 100x100 μm and 93x93 nodes. The reason for the ANS liner measurement being of a smaller size than the other measurements was that the density of the deep honing grooves made it impossible to select an area of 150x150 μm without including some of them, in the measurement aperture. Therefore, a smaller area was chosen to keep the measurement representative of the plateau surface only.

The average roughness parameter, R_a , Elastic Modulus and Poisson's ratio for these four surfaces as well as the opposing piston ring surface are summarised in Table 3.

The first surface, denoted as 'STD55', is a standard production grey cast iron cylinder liner with a honing angle of 55° and $R_a = 0.196 \mu m$. The second surface, 'STD35' is also a grey cast iron cylinder liner, but with a honing angle of 35° and a slightly rougher surface finish of $R_a = 0.263 \mu m$. The third surface, denoted 'ANS' is a grey cast iron cylinder liner treated with ANS Triboconditioning®. This process is incorporated into the honing process with the use of a special honing tool and fluid [27, 28]. A layer of Tungsten Disulphide (WS_2) is deposited on the surface and the topography is also modified to give a more run-in like surface finish, where $R_a = 0.132 \mu m$. The final surface, denoted 'PL', is a grey cast iron liner that is plasma sprayed with a stainless steel and ceramic composite before being honed with a very small grit size tool which

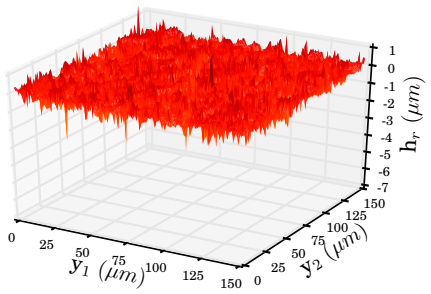

(a) STD55.

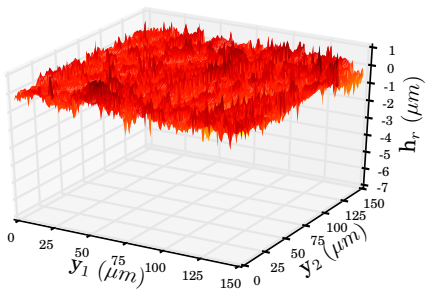

(b) STD35.

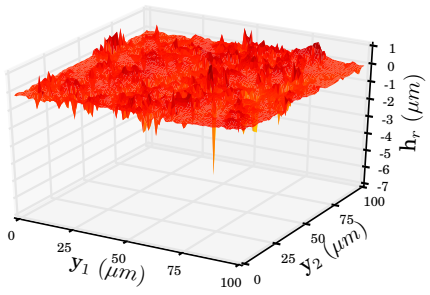

(c) ANS.

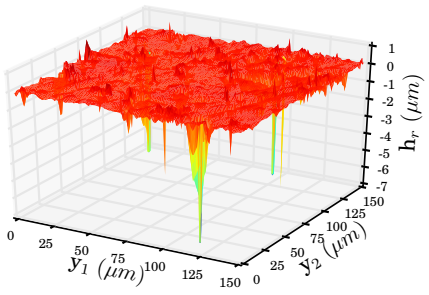

(d) PL.

Figure 3: Surface images.

leaves an approximately 100μm thick coating of stainless steel on the surface with a low roughness of $R_a = 0.138\mu m$. The surface is also relatively porus with deep holes in the stainless steel rather than deep honing grooves of the STD55, STD35 and ANS surfaces.

4.1 Calculation of flow factors and asperity contact pressures

When solving the force balance, equation (9), asperity contact pressure as a function of separation is required. Also, as discussed in Section §3, homogenized coefficients are used to include the effects of surface roughness when solving equation (4) over the smooth global domain and must be calculated too. The calculation of these parameters for the surfaces illustrated in Figure 3 is now discussed.

When the surfaces come into contact, the deformation and asperity contact pressure are found using an fft-accelerated, boussinesq-type elasto-plastic contact mechanics model. This model, unlike the more common approach by Greenwood and Tripp [29], numerically deforms a real, measured, surface topography to give the average asperity contact pressure as a function of separation. The technique is described in detail by Sahlin et al. [30, 31] and will not be repeated here. The piston ring, $R_a = 0.066\mu$m, is rather smooth compared to the liner surfaces and is therefore assumed to perfectly smooth during the numerical simulations. The deformation and asperity contact pressure results are thus obtained by loading a smooth surface against the roughness measurements depicted in Figure 3. These surface measurements, described in Section §4, were interpolated onto a 512x512 grid before being input into the contact mechanics

Table 3: Roughness parameters and dry friction coefficients for each cylinder liner sample.

Sample	Ra (μm)	Friction coefficient (μ)	Elastic modulus (GPa)	Poisson's ratio
STD55	0.196	0.1274	140	0.3
STD35	0.263	0.1249	140	0.3
ANS	0.132	0.1142	140	0.3
PL	0.138	0.1115	140	0.3
Piston Ring	0.066	N/A	220	0.3

model. To calculate the asperity contact pressure, the elastic modulus and Poisson's ratio of each of the surfaces is needed. These values are given in Table 3. In the model plastic deformation is assumed to occur if the local asperity contact pressure exceeds 1% of the elastic modulus. The resulting asperity contact pressure as a function of average separation between the surfaces is given for the standard liner surface in Figure 4.

To take into account the effect of the surface roughness, the homogenized coefficients A_0, B_0 and $\bar{h}$ are calculated. For each of the surfaces in Figure 3, the following Partial Differential Equations (PDE's),

$$\nabla_y \cdot \left(h^3 \nabla_y \psi_1\right) = 0 \text{ in } Y, \tag{13}$$

$$\begin{aligned} \psi_1(x,0,y_2) + 1 &= \psi_1(x,l_1,y_2), \\ \psi_1(x,y_1,0) &= \psi_1(x,y_1,l_2). \end{aligned}$$

$$\nabla_y \cdot \left(h^3 \nabla_y \psi_2\right) = 0 \text{ in } Y, \tag{14}$$

$$\begin{aligned} \psi_2(x,0,y_2) &= \psi_2(x,l_1,y_2), \\ \psi_2(x,y_1,0) + 1 &= \psi_2(x,y_1,l_2). \end{aligned}$$

$$\nabla_y \cdot \left(h^3 \nabla_y \chi_0\right) = \nabla_y \cdot (h e_1) \text{ in } Y, \tag{15}$$

$$\begin{aligned} \chi_0(x,0,y_2) &= \chi_0(x,l_1,y_2), \\ \chi_0(x,y_1,0) &= \chi_0(x,y_1,l_2). \end{aligned}$$

are solved with periodic boundary conditions in both the y_1 and y_2 directions over the measurement domain, i.e., the cell of periodicity, $Y = (0,l_1) \times (0,l_2)$, where h describes the clearance between the rough surfaces and ψ_1, ψ_2 and χ_0 are local scale variables. Instead of solving these equations for each pair of values $x = (x_1, x_2) \in \Omega$, they are solved for a range of separations, α, defined as the distance between the rough surface and the smooth counter-surface (the piston ring). Mathematically:

$$h = h_r + \alpha, \tag{16}$$

where h_r represents the surface roughness (Figure 3). In order to obtain sufficiently well resolved homogenized coefficients, α is taken as a range of distances between 0.1-55 μm.

Once ψ_1, ψ_2 and χ_0 have been calculated they can be integrated/averaged to give the homogenized coefficients A_0, B_0 and $\bar{h}$ in equation (4) needed to solve the averaged form of the Reynolds equation. The explicit expressions for the coefficients A_0, B_0 and $\bar{h}$ read:

$$a_{11}(x) = \frac{1}{l_2} \int_Y h^3 \frac{\partial \psi_1}{\partial y_1} dy, \tag{17}$$

$$a_{12}(x) = \frac{1}{l_1} \int_Y h^3 \frac{\partial \psi_2}{\partial y_1} dy, \tag{18}$$

$$a_{21}(x) = \frac{1}{l_2} \int_Y h^3 \frac{\partial \psi_1}{\partial y_2} dy, \tag{19}$$

$$a_{22}(x) = \frac{1}{l_1} \int_Y h^3 \frac{\partial \psi_2}{\partial y_2} dy, \tag{20}$$

$$\begin{pmatrix} b_1(x) \\ b_2(x) \end{pmatrix} = \frac{1}{l_1 l_2} \int_Y h e_1 - h^3 \nabla_y \chi_0 dy, \tag{21}$$

while $\bar{h}$ is defined in equation (7). The results of these calculations for a_{11}, a_{22} and b_1 for the STD55 surface are shown in Figure 4.

5 Results and Discussion

In the following sections, friction and film thickness results from both the numerical model and experimental setup will be presented and compared.

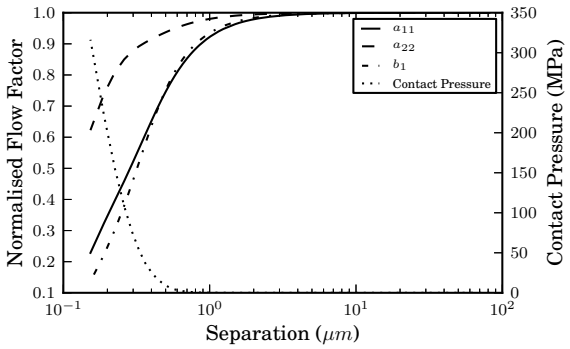

Figure 4: Asperity Contact Pressures and Flow Factors for the STD55 liner.

Finally, there will be a deep-dive into selected results to investigate the similarities and differences between the numerical and experimental film thickness and friction in a time resolved format.

5.1 Friction

In Figure 5, the friction coefficient averaged through the reciprocating cycle is presented for each of the four surfaces. On each plot both the experimental values and the simulated values are given.

Figure 5a gives the friction map for the STD55 surface. It can be observed that the correlation between the measured and numerically predicted film thickness is very good, with the two surfaces sitting almost exactly on top of each other. As would be expected, the friction coefficient is highest at 200 N and 2.5 Hz, i.e. the highest load and lowest speed. The physical explanation is that the entraining speed is insufficient to generate an oil film to support such a high load. A friction coefficient of around 0.1 at this point suggests a majority of boundary lubrication, as the dry friction coefficient was found to be 0.1274 for the standard surface (see Table 3). However, it should be remembered that this is a reciprocating test and therefore the lubrication regime will vary throughout the stroke. This will be investigated further in the following sections where film thickness is evaluated and the friction contributions divided into boundary and viscous components. Looking at the rest of the friction map, as the speed increases, or the load reduces, the average friction coefficient drops in value. This indicates moving further to the right on the Stribeck curve as lower load, or higher speed, allows for a thicker oil film to be generated and the majority lubrication regime becomes either mixed or full film rather than boundary. The lowest average friction coefficient occurs at the lightest load and highest speed; 40 N and 17.5 Hz. Here the thickest film is observed and the asperity friction contributes the least to the total friction. Overall, the simulation slightly overestimates the friction coefficient. There are a number of reasons for this, e.g., the viscosity or boundary friction coefficient used in the simulation could be slightly higher than what it actually was during the experiment. It is reasonable to assume that the shear heating of the lubricant during the test, could raise the oil temperature and lower its viscosity, thereby reducing the viscous friction compared to that predicted by the numerical simulation. The only exception to the simulation having slightly higher values for the STD55 liner (5a) is at 40 N load, where the experimental friction coefficient seems to increase from 60 N and become slightly larger than the simulated value. It is suggested that this could be caused by the friction force sensor detector limit in the experiment. At 40 N, the friction force is very small (40 N multiplied by a friction coefficient of around 0.02) and it may be too small for the friction force sensor to be accurately recorded.

Moving onto the STD35 sample and the results presented in Figure 5b. The simulated friction map, for this surface, is found to have marginally higher values than the STD55 liner. This occurs because the surface is slightly rougher exhibiting an R_a value of 0.263 μm as opposed to 0.196 μm for the STD55 surface. This means that for the same operating conditions the surfaces come into direct contact sooner, which results in a higher percentage of boundary friction. However, when comparing the friction maps for the measured data, the STD35 liner exhibits lower friction as the load increases in comparison to the STD55 liner. There are two proposed explanations for this. Firstly, the reduction in honing angle (from STD55 to STD35) could have increased the oil film thickness, as shown by Jocsak et al. [32] and thereby reduced both the viscous shear of the lubricant and likelihood of boundary lubrication, which in turn cancels out the increase in surface roughness. The surface roughness measurements, depicted in Figure 3, only contain an

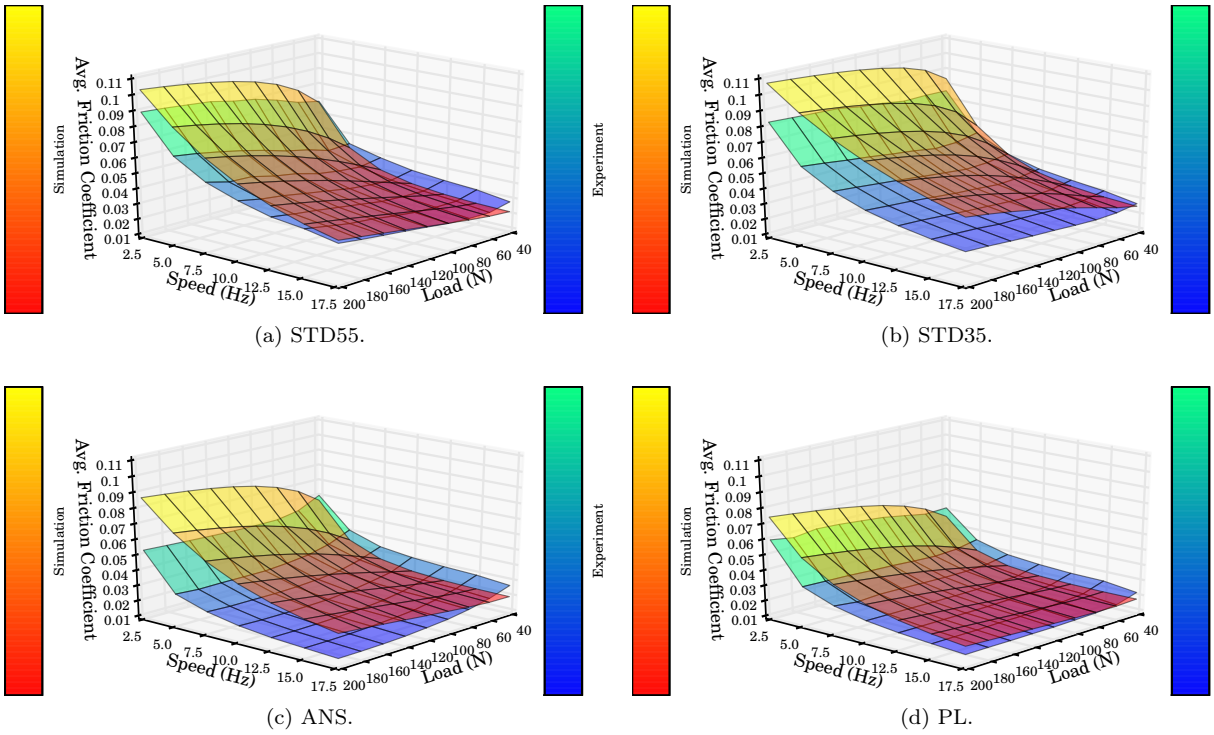

(a) STD55.

(b) STD35.

(c) ANS.

(d) PL.

Figure 5: Average friction coefficient maps.

area of the plateau region with no major honing grooves. This means that the effect from the honing angle is not considered fully in the numerical simulations. This is the reason why the effect of honing angle, appears in the measured friction data and not in the data predicted by the simulation. Secondly, and along the same lines, the surface roughness could have helped the formation of an oil film by contributing to the converging gap in the inlet. This would also help increase the oil film thickness and cancel out the effect of a rougher surface. This would also not be predicted by the simulations, because the roughness is only considered in the local scale and no inter-asperity cavitation, and therefore no lift, is generated.

The third friction map, shown in Figure 5c, presents the data for the ANS (Triboconditioning®) surface. This surface, along with the final plasma coated surface, PL, with friction map in Figure 5d, shows significantly lower average friction coefficients than the STD55 and the STD35 liner surfaces, across the whole friction map. This is predominately due to the reduction in surface roughness, which at 0.132 μm is merely half that of the STD55 liner and half of the STD35 liner. The boundary friction coefficient, although lower due to the Tungsten Disulphide coating, is broadly similar to that of the STD55 liner (0.1142 for the ANS liner compared to 0.1274 for the STD55 liner). The simulation predicts friction coefficients less than the STD55 and the STD35 surfaces, however the experimental friction coefficients are even lower. The slight increase in friction at 40N load is, as previously suggested, most likely due to the friction sensor detector limit.

The final friction map, i.e. the one in Figure 5d, presents data for the plasma coated liner (PL). Here the simulation and experimental data match very well. The friction coefficient is very low, like with the ANS liner most likely because of the small R_a value of 0.138 μm. The boundary friction coefficient of 0.1115 is less than the STD55 and STD35 liners but not significantly so. The smoother sur-

face provides for full film lubrication at lower speeds and higher loads and delays the onset of boundary lubrication as the speed reduces or the load increases.

5.2 Film thickness

In this section, the numerically simulated film thickness and the film thickness measured with ultrasound will be compared. Figure 6, presents the numerically and experimentally obtained film thickness data, for the STD55, STD35 and ANS liner. There is no data for the plasma liner. This is because the ultrasound technique was not able to measure the film thickness through the plasma coating due to attenuation of the ultrasound signal in the coating.

In each subfigure, seven surfaces are plotted, one for each of the sliding speeds, with position on the x and load on the y axes. Only one sliding direction can be shown, in all cases this is from the left to the right of the image in Figure 1, with the ring orientated in the direction shown in Figure 2. The stroke in the other direction, from right to left, was not considered due to potential anomalies in the ultrasound measurement due to cavitation. This effect is discussed in great detail in a previous work by the same authors [8]. The simulated film thickness maps, contain 50 steps for each stroke. As was discussed in Section 2.2 and illustrated in Figure 1, the ultrasound technique measured the film thickness at five discrete locations on the cylinder liner surface, therefore the experimental plots have five points for each stroke. On the z axis the Minimum Oil Film Thickness (MOFT) is given. At a given sensor position this is the smallest film thickness that occurs between the cylinder liner surface and the piston ring as the ring passes over the sensor. A deconvolution operation is performed to get the 'true' minimum rather than the average over the sensor width. This has already been explained in [8]. In the simulations, the definition of MOFT is the distance between the mean plane of the surface roughness and the (smooth) ring profile.

All plots show the same trend in film thickness, where the MOFT increases towards the mid-stroke - as the entraining speed increases, and then reduces - as the ring comes to a halt at the end of the stroke. The film thickness maps, from simulations and experiments, are all skewed so that the maximum MOFT occurs just past mid-stroke, where the entraining speed is greatest. This is due to the time dependent nature of the oil film build-up, and time dependence is also considered when solving the modified Reynolds equation, equation (4), during the numerical simulation.

At low speeds the simulated and experimental film thicknesses, for all three liner surfaces, compare well. According to the ultrasound measurements, the ANS coated liner surface seems to generate a lower film thickness than the other two liners and this is also what the numerical simulation predicts. There is a greater difference at higher speeds where measured film thickness is significantly lower that the value computed by the model. Due to the fact that the experimentally measured and numerically simulated friction compare very well at this point, see Figure 5a, it is suggested that this difference occurs because the ultrasonic film thickness measurement is underestimating the film thickness. At high speeds more cavitation occurs in the trailing portion of the contact, as shown by Dellis and Arcoumanis [33] and also from the results of the numerical model. Unfortunately, the effect of cavitation on the speed of sound and density in a medium confined between two surfaces in relative motion has, to the authors' knowledge not yet been researched. However, these properties are needed to translate the measured reflection coefficient into film thickness, using equation (3), and the uncertainty in these values could lead to the errors in film thickness measurement at high speed.

5.3 Time resolved data analysis

Five load and speed combinations will be investigated in more detail here. These are listed in Table 4. Four of the test points represent the corners of the speed/load map and the fifth is in the middle, giving three points which are predominantly mixed lubrication, one boundary lubrication and one full-film. The lowest load chosen is 60 N rather than 40 N, due to the potential inaccuracy in the friction force sensor at 40 N as discussed in Section 5.1. For each test point the STD55 and PL liner will be investigated further. These liners were chosen for two reasons - firstly the STD55 liner is one of the higher friction surfaces and the plasma a lower friction surface so differences should be apparent, and secondly because these two liners are

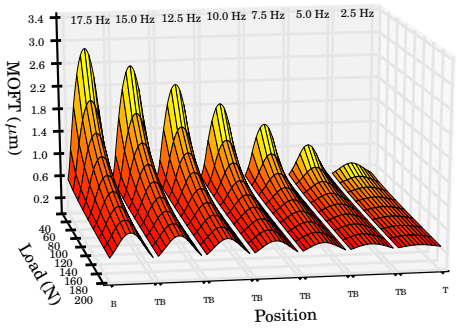

(a) STD55 Simulation.

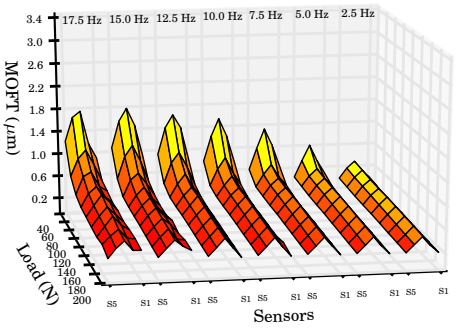

(b) STD55 Experiment.

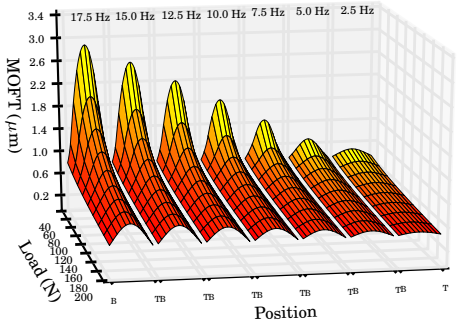

(c) STD35 Simulation.

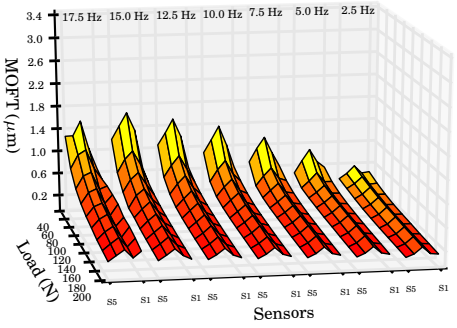

(d) STD35 Experiment.

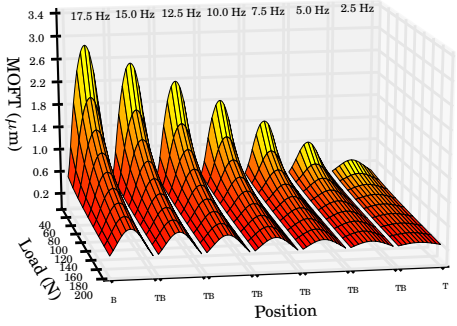

(e) ANS Simulation.

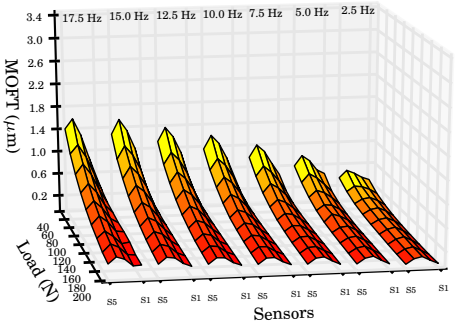

(f) ANS Experiment.

Figure 6: Film thickness comparison of three liner samples (for sensor positions refer to Figure 1). 'T' refers to the reversal point closest to the load cell and 'B' refers to the reversal point closest to the reciprocating arm.

Table 4: Deep dive test points.

Test	Lub. Regime	Load (N)	Speed (Hz)
1	Full Film	60	17.5
2	Mixed	200	17.5
3	Mixed	60	2.5
4	Mixed	120	10.0
5	Boundary	200	2.5

production surfaces, while the STD35 and ANS liners are prototype surfaces. The friction data for the STD55 and the PL liner will be further investigated by looking at the boundary and the viscous friction, for the five speed and load combinations independently. The data will also be examined in a time resolved manner.

The simulated friction is split into viscous and boundary friction components for each of the test points. The results are given in Figure 7. It is interesting to see the contributions from the viscous and boundary friction so that when the time resolved data is discussed, the results can be better understood.

The lubrication regime of the first point, 60 N and 17.5 Hz, is predominantly hydrodynamic. The split between viscous and boundary friction is approximately 50/50, with most of the boundary contribution occurring near the reversal points and the mid-stroke being mostly hydrodynamic. The second test point, i.e. 200 N and 17.5 Hz, shows a similar viscous friction component but greatly increased boundary friction. This is not so surprising, since the high entraining speed is maintained, leading to similar viscous friction, albeit slightly increased due to the higher load reducing the film thickness and thereby increasing viscous shear. The increased load also leads to more severe boundary lubrication at the reversal points. In the third test point; 60 N and 2.5 Hz, the contact is operating almost exclusively in the boundary lubrication regime. The reason for this is the very low entraining speed inhibiting the formation of a significant hydrodynamic pressure profile and generation of hydrodynamic lift. The boundary friction contribution at the fourth test point; 120 N and 10.0 Hz, is similar to the one in test point 3. The increased load, reducing film thickness, is offset by a greater entraining speed which will allow a greater hydrodynamic film to be generated. The viscous shear

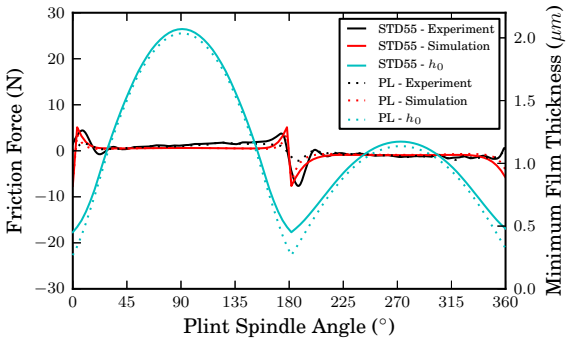

Figure 8: Test Point 1 - 60 N and 17.5 Hz.

is much greater, however, due to the increased entraining speed. In the final test point; 200 N and 2.5 Hz, the friction force is composed almost entirely from boundary friction, due to the very high load and low entraining speed. The average friction force for the STD55 liner of just over 20 N, is almost equal in magnitude to the applied load of 200 N multiplied by the friction coefficient of 0.1274. This indicates very little contribution to load support by hydrodynamic film generation.

In the majority of the test cases, it can be observed that the friction force is dominated by boundary friction. However, it must be remembered that the power loss, which is what we are really interested in, is equal to friction force multiplied by velocity. As the majority of the boundary friction occurs around the reversal points (where the velocity is very low) and most viscous friction occurs at mid-stroke (when the velocity is, relatively, much higher) then the viscous contribution to power loss is much greater.

Figure 8, shows the friction and film thickness for the first test point; 60 N and 17.5 Hz. In this plot, and in all following plots, the solid lines are for the STD55 liner and the dashed lines are for the plasma liner. The x-axis gives the Plint crank angle.

There is little difference between the STD55 and PL liner surfaces. A physical explanation to is that the surface topography only very weakly influences the total friction in the full film lubrication regime. The film thickness is greater between 0-180° due to the longer converging gap in that direction (see Figure 2).

The second test point, with time resolved friction

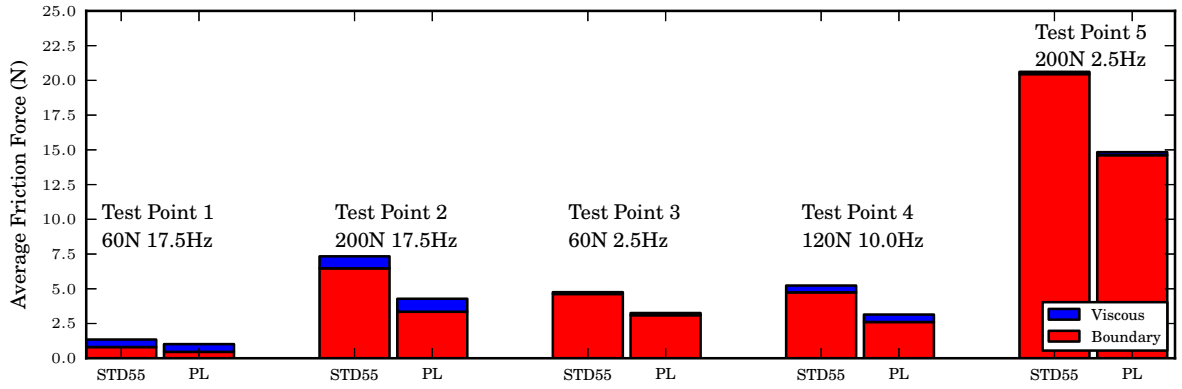

Figure 7: Breakdown of simulated friction into viscous and boundary components.

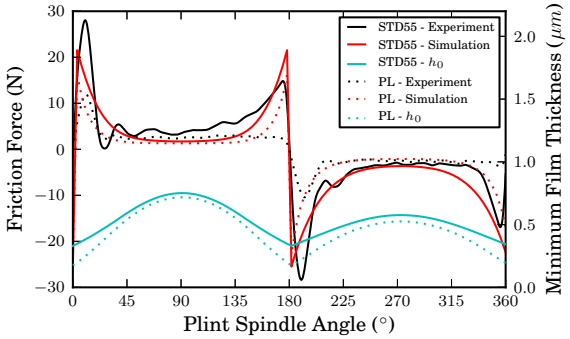

Figure 9: Test Point 2 - 200 N and 17.5 Hz.

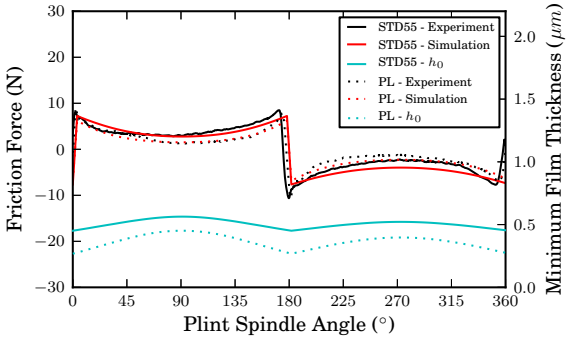

Figure 10: Test Point 3 - 60 N and 2.5 Hz.

data in Figure 9, is for 200 N and 17.5 Hz, which is the highest speed and highest load. Under these conditions the contact has entered the mixed lubrication regime. At the reversal points, the friction is very high with virtually all of the load supported by the asperities. For the STD55 liner, with no hydrodynamic film generated, the friction force is almost equal to the normal load of 200 N, multiplied by the dry friction coefficient, found in Table 3. With a smoother surface, the PL liner maintains an oil film with less asperity contact and some of the load is always supported by hydrodynamic lubrication, giving a considerably lower friction coefficient at the reversal points. Even at mid-stroke the lubrication regime for the STD55 liner never becomes fully hydrodynamic and so this explains the larger friction force compared to the PL liner here. The simulated and measured results compare well. The only significant difference is that the simulation overestimates the friction for the PL liner at the reversal points, suggesting that the onset of asperity contact occurs sooner in the simulation.

The time resolved data for the third test point - 60 N and 2.5 Hz, which is the lowest load and lowest speed is presented in Figure 10. As in the previous test point, the contact operates in mixed lubrication although with a lower friction force than in the previous test point. Figure 10, reveals that boundary lubrication occurs at the reversal points, just as in Figure 9, however the reduction in friction at mid-stroke is less significant. This is due to the seven times lower entraining speed. The measured and simulated friction force match extremely well, with the same trend for lower friction from the plasma liner echoed in both results.

The friction and film thickness data for the fourth

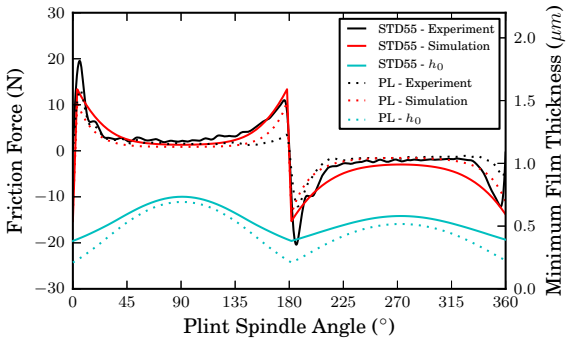

Figure 11: Test Point 4 - 120 N and 10.0 Hz.

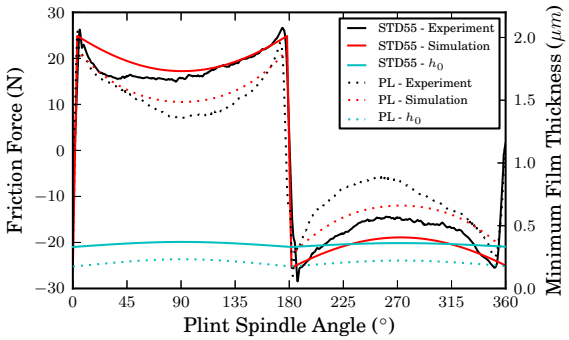

Figure 12: Test Point 5 - 200 N and 2.5 Hz.

test point is depicted in Figure 11. This point is for medium speed and medium load; 120 N and 10.0 Hz which places the contact predominantly in the mixed regime. The friction force plot and film thicknesses are broadly similar to that of test point 2, shown in Figure 9. The friction force is lower because the applied load is lower - 120 N instead of 200 N, but the behaviour is almost identical. The reason is that, although the load is less, the entraining speed to generate an oil film is also less.

The final test point; 200 N and 2.5 Hz, places the contact predominantly in the boundary lubrication regime, as illustrated in Figure 12. It can be observed that the increase in film thickness throughout the stroke is minimal. There is a minor reduction in friction force at the mid-stroke, however it is still very high and comes mainly from asperity friction. Thus the contact operates predominantly in boundary lubrication. In both the measured and simulated result there is lower friction with the plasma liner. The smoother surface of the plasma liner leads to lift-off occurring sooner, as the entraining speed increases away from the mid-stroke. This is increasing the hydrodynamic load support and reducing the asperity contact with lowered boundary friction as a result.

6 Conclusions

The friction between a piston ring and cylinder liner has been investigated for four different cylinder liner variants. A reciprocating test rig was used to simulate the contact and both friction and oil film thickness, measured with ultrasound, was recorded by means of a specially designed experimental setup. Moreover, a numerical model was developed and implemented to calculate friction and film thickness and comparisons were made between the experimentally measured and numerical results. The following conclusions are drawn:

- Both measured and simulated friction and film thickness, could be used to clearly differentiate between the investigated surfaces.
- The cylinder liner variants with lower surface roughness, i.e. the ANS and plasma liners, exhibited significantly lower friction, according to both the measurements and the simulations.
- The results for friction from the numerical model and experiment compared well, with similar trends and magnitudes for both.
- At low speeds the measured friction and film thicknesses were very similar. However, at higher speeds the simulation predicts a larger film thickness than that observed in the experiment. Due to the good correlation between the measured and simulated friction, it is proposed that this difference is due to imprecise values of lubricant density and speed of sound in the lubricant, caused by increased lubricant cavitation, being used when processing the ultrasound data.

7 Acknowledgements

Scania AB is thanked for providing components, technical data and discussions. Applied Nano Surfaces is thanked for allowing the publication of this

work and providing the ANS Triboconditioning® cylinder liner. Loughborough University are thanked for performing the surface measurements of the cylinder liner samples.

8 Funding

The authors from the Leonardo Centre would like to acknowledge the EPSRC Encyclopaedic Program Grant for funding their contribution to this work. Support of all the program industrial partners is acknowledged. The authors from LTU would like to thank Stiftelsen för Strategisk Forskning (SSF) and ProViking for funding their contribution to this work and the Swedish Research School in Tribology for funding Andrew Spencer's placement at Sheffield University.

Nomenclature

$\bar{h}$	Average film thickness (m)
χ_0	Local scale variable
η	Lubricant viscosity (Pa · s)
γ	12 η
λ	$6\eta U$
μ	Dry friction coefficient
ω	Angular frequency (rad/s)
ψ_1	Local scale variable
ψ_2	Local scale variable
ρ	Density of lubricant (kg/m^3)
ρ_c	Cavitation density of lubricant (kg/m^3)
θ	Plint spindle angle (°)
A	ASTM D31 lubricant constant
A_0	Pressure flow factor matrix
a_{xx}	Pressure flow factor
B	ASTM D31 lubricant constant
B	Bulk Modulus (Pa)
B_0	Shear flow factor matrix
b_{xx}	Shear flow factor
c	Speed of sound in lubricant (m/s)
f	Frequency of ultrasonic pulse (Hz)
f_{bd}	Boundary friction force (N)
F_{CP}	Asperity contact load (N)
F_{HYD}	Hydrodynamically supported load (N)
f_{hyd}	Viscous friction force (N)
f_{tot}	Total friction force (N)
h	Oil film thickness (m)
h_0	Separation between piston ring and cylinder liner (m)
h_r	Liner roughness amplitude (m)
K	Stiffness (N/m)
$l_{1/2}$	Length/width of roughness sample (m)
N	Rotational speed of Plint (Hz)
p_0	Averaged film pressure (Pa)
P_{CP}	Asperity Contact Pressure (Pa)
R	Reflection coefficient
r	Cavitation algorithm complementary variable
R_a	Average roughness parameter (μm)
s	Stroke (m)
T	Temperature (°C)
U	Entraining speed (m/s)
$x_{1/2}$	Global scale coordinates (m)
$y_{1/2}$	Local scale coordinates (m)
z	Acoustic impedence (N/s/m^3)

References

[1] Exxon Mobil. 2012 the outlook for energy: A view to 2040. Technical report, Exxon Mobil, 2012.

[2] European Commission. White paper - roadmap to a single european transport area - towards a competitive and resource efficient transport system. Technical report, 2011.

[3] D.E. Richardson. Review of power cylinder friction for diesel engines. *Transactions of the ASME: Journal of Engineering for Gas Turbines and Power*, 122:506–519, 2000.

[4] S.K. Michail and G.C. Barber. The effects of roughness on piston ring lubrication Part 1: Model development. *STLE: Tribology Transactions*, 38:19–26, 1995.

[5] S.K. Michail and G.C. Barber. The effects of roughness on piston ring lubrication Part 2: The relationship between cylinder wall surface topography and oil film thickness. *STLE: Tribology Transactions*, 38:173–177, 1995.

[6] A. Johansson, P.H. Nilsson, R. Ohlsson, C. Anderberg, and B-G. Rosén. New cylinder liner surfaces for low oil consumption. *Tribology International*, 41:854–859, 2008.

[7] O. Sato, M. Takiguchi, T. Aihara, Y. Seki, K. Fujimura, and Y. Tateishi. Improvement of piston lubrication in a diesel engine by means of cylinder surface roughness. *SAE Technical Paper Series*, 2004-01-0604:1–7, 2004.

[8] E. Y. Avan, A. Spencer, R. Dwyer-Joyce, A. Almqvist, and R. Larsson. Experimental and numerical investigations of oil film formation and friction in a piston ring-liner contact. *IMechE Part J: Journal of Engineering Tribology*, Online First:1–15, 2012.

[9] S.J. Söchting and I. Sherrington. The effect of load and viscosity on the minimum operating oil film thickness of piston-rings in internal combustion engines. *Proceedings of the Institution of Mechanical Engineers, Part J: Journal of Engineering Tribology*, 223:383–391, 2009.

[10] D.O. Ducu, R.J. Donahue, and J.B. Ghandhi. Design of capacitance probes for oil film thickness measurements between the piston ring and linear in internal combustion engines. *Journal of Engineering for Gas Turbines and Power*, 123:633–643, 2001.

[11] A. Dhar, A.K. Agarwal, and V. Saxena. Measurement of dynamic lubricating oil film thickness between piston ring and liner in a motored engine. *Sensors and Actuators, A: Physical*, 149:7–15, 2009.

[12] P. Saad, L. Kamo, M. Mekari, W. Bryzik, V. Wong, N. Dmitrichenko, and R. Mnatsakanov. Modeling and measurement of tribological parameters between piston rings and liner in turbocharged diesel engine. *SAE Technical Paper Series*, 2007-01-1400:1–16, 2007.

[13] T. Seki, K. Nakayama, T. Yamada, A. Yoshida, and T. Takiguchi. A study on variation in oil film thickness of a piston ring package: variation of oil film thickness in piston sliding direction. *JSAE Review*, 21:315–320, 2000.

[14] M. Takiguchi, K. Nakayama, S. Furuhama, and H. Yoshida. Variation of piston ring oil film thickness in an internal combustion engine - comparison between thrust and anti-thrust sides. *SAE paper No. 980563*, 980563, 1998.

[15] R.I. Taylor and P.G. Evans. In-situ piston measurements. *Proc. IMechE Part J: Engineering Tribology*, 218:185–200, 2004.

[16] P. Harper, R.S. Dwyer-Joyce, U. Sjödin, and U. Olofsson. Evaluation of an ultrasonic method for measurement of oil film thickness in a hydraulic motor piston ring. In *Proceedings of the 31st Leeds-Lyon Symposium on Tribology*, 2004.

[17] E.Y. Avan, R.S. Mills, and R.S. Dwyer-Joyce. Ultrasonic imaging of the piston ring oil film during operation in a motored engine - towards oil film thickness measurement. *SAE International Journal of Fuels and Lubricants*, 3(2):786–793, 2010.

[18] R.S. Mills, E.Y. Avan, and R.S. Dwyer-Joyce. Piezoelectric sensors to monitor lubricant film

thickness at piston-cylinder contacts in a fired engine. *Proc. IMechE Part J: Engineering Tribology*, 227:100–111, 2013.

[19] N.W. Bolander, B.D. Steenwyk, F. Sadeghi, and G.R. Gerber. Lubrication regime transitions at the piston ring-cylinder liner interface. *Proc. IMechE Part J: Engineering Tribology*, 219:19–31, 2005.

[20] R.S. Dwyer-Joyce, B.W. Drinkwater, and C.J. Donohoe. The measurement of lubricant-film thickness using ultrasound. *Proceedings of the Royal Society A: Mathematical, Physical and Engineering Sciences*, 459:957–976, 2003.

[21] M. Giacopini, M. T. Fowell, D. Dini, and A. Strozzi. A mass-conserving complementarity formulation to study lubricant films in the presence of cavitation. *ASME: Journal of Tribology*, 132:1–12, 2010.

[22] G. Bayada, M.E.A. Talibi, and K.A. Hadi. Existence and uniqueness for a non-coercive lubrication problem. *Journal of Mathematical Analysis and Applications*, 327:585–610, 2007.

[23] R.W. Cottle, J-S. Pang, and R. Stone. *The Linear Complementarity Problem*. Society for Industrial & Applied Mathematics, 2009.

[24] D. Kroshko. OpenOpt: Free scientific-engineering software for mathematical modeling and optimization. software package downloadable from http://openopt.org, 2013.

[25] N. Morris, R. Rahmani, H. Rahnejat, P.D. King, and B. Fitzsimmons. Tribology of piston compression ring conjunction under transient thermal mixed regime of lubrication. *Tribology International*, 59:248–258, 2013.

[26] A. Spencer, A. Almqvist, and R. Larsson. A semi-deterministic texture-roughness model of the piston ring-cylinder liner contact. *Proc. IMechE Part J: J. Engineering Tribology*, 225:1–9, 2011.

[27] B. Zhmud, G. Flores, C. Verpoort, and U. Morawitz. A novel surface finishing process for improving tribological properties of cylinder bores. In *Proc. 6th VDI-Conference Zylinderlaufbahn, Kolben, Pleuel*, 2012.

[28] B. Zhmud, E-B. Åkerlund, S. Jacobson, J. Hardell, L. Hammerström, and R. Ohlson. Ans triboconditioning: In-manufacture running-in process for improving tribological properties of mechanical parts made of steel or cast iron. In *Proc. 18th International Colloquium Tribology - Industrial and Automotive Lubrication*, 2012.

[29] J.A. Greenwood and J.H. Tripp. The contact of two nominally flat rough surfaces. *Proc. IMechE*, 185:625–633, 1971.

[30] F. Sahlin, Larsson. R., A. Almqvist, P.M. Lugt, and P. Marklund. A mixed lubrication model incorporating measured surface topography Part 1: theory of flow factors. *Proc. IMechE Part J: Journal of Engineering Tribology*, 224:335–351, 2010.

[31] F. Sahlin, R. Larsson, P. Marklund, A. Almqvist, and P.M. Lugt. A mixed lubrication model incorporating measured surface topography Part 2: roughness treatment, model validation, and simulation. *Proc. IMechE Part J: Journal of Engineering Tribology*, 224:353–365, 2010.

[32] J. Jocsak, Y. Li, T. Tian, and V.W. Wong. Modeling and optimizing honing texture for reduced friction in internal combustion engines. *SAE Technical Paper Series*, 2006-01-0647:1–15, 2006.

[33] P. Dellis and C. Arcoumanis. Cavitation development in the lubricant film of a reciprocating piston-ring assembly. *Proc. IMechE Part J: J. Engineering Tribology*, 218:157–171, 2004.